

## Chemical and valence reconstruction at the surface of SmB<sub>6</sub> revealed by means of resonant soft x-ray reflectometry

V. B. Zabolotnyy,<sup>1,\*</sup> K. Fürsich,<sup>1,†</sup> R. J. Green,<sup>2,3</sup> P. Lutz,<sup>4</sup> K. Treiber,<sup>4</sup> Chul-Hee Min,<sup>4</sup> A. V. Dukhnenko,<sup>5</sup> N. Y. Shitsevalova,<sup>5</sup> V. B. Filipov,<sup>5</sup> B. Y. Kang,<sup>6</sup> B. K. Cho,<sup>6</sup> R. Sutarto,<sup>7</sup> Feizhou He,<sup>7</sup> F. Reinert,<sup>4</sup> D. S. Inosov,<sup>8</sup> and V. Hinkov<sup>1</sup>

<sup>1</sup>*Experimentelle Physik IV and Röntgen Center for Complex Materials Systems (RCCM), Universität Würzburg, Am Hubland, 97074 Würzburg, Germany*

<sup>2</sup>*Stewart Blusson Quantum Matter Institute, Department of Physics & Astronomy, University of British Columbia, 2355 East Mall, Vancouver, Canada V6T 1Z4*

<sup>3</sup>*Department of Physics & Engineering Physics, University of Saskatchewan, Saskatoon, Saskatchewan, Canada S7N 5E2*

<sup>4</sup>*Experimentelle Physik VII and Röntgen Center for Complex Materials Systems (RCCM), Universität Würzburg, Am Hubland, 97074 Würzburg, Germany*

<sup>5</sup>*I. M. Frantsevich Institute for Problems of Materials Science of NAS, 3 Krzhynzhovskyy Street, Kiev 03680, Ukraine*

<sup>6</sup>*School of Materials Science and Engineering, Gwangju Institute of Science and Technology, Gwangju 500-712, Korea*

<sup>7</sup>*Canadian Light Source Inc., Saskatoon, Saskatchewan, Canada S7N 2V3*

<sup>8</sup>*Institut für Festkörper- und Materialphysik, TU Dresden, D-01069 Dresden, Germany*



(Received 14 December 2017; revised manuscript received 19 March 2018; published 14 May 2018)

Samarium hexaboride (SmB<sub>6</sub>), a Kondo insulator with mixed valence, has recently attracted much attention as a possible host for correlated topological surface states. Here, we use a combination of x-ray absorption and reflectometry techniques, backed up with a theoretical model for the resonant  $M_{4,5}$  absorption edge of Sm and photoemission data, to establish laterally averaged chemical and valence depth profiles at the surface of SmB<sub>6</sub>. We show that upon cleaving, the highly polar (001) surface of SmB<sub>6</sub> undergoes substantial chemical and valence reconstruction, resulting in boron termination and a Sm<sup>3+</sup> dominated subsurface region. Whereas at room temperature, the reconstruction occurs on a timescale of less than 2 h, it takes about 24 h below 50 K. The boron termination is eventually established, irrespective of the initial termination. Our findings reconcile earlier depth resolved photoemission and scanning tunneling spectroscopy studies performed at different temperatures and are important for better control of surface states in this system.

DOI: [10.1103/PhysRevB.97.205416](https://doi.org/10.1103/PhysRevB.97.205416)

### I. INTRODUCTION

SmB<sub>6</sub> has been extensively studied for more than 50 years. Originally, it had drawn scientific interest as a mixed valence system [1–11], later as a Kondo insulator [12–14]. More recently, when topological insulators started arresting the attention of a substantial part of the solid state community, the material has become famous again as a potential topological Kondo insulator, in which surface states with unusual properties are to be observed [15–20].

Obviously, for any surface state, *be it topological or not*, the structure and the composition of the surface play an important role. While removal of trivial surface states via surface disorder became an everyday tool, influencing a topologically protected state may seem unexpected at first. However, it should be remembered that “topological protection” holds against some continuous (“adiabatic”) changes that do not close the bulk gap. In the cases where disorder forms within a thin layer at the surface, one can still see how the topological state

is expelled into the undisrupted bulk of the material. Nice illustration for this can be found in the experimental work of Queiroz *et al.* [21], where the authors were able to demonstrate a sputtering-induced recurrence of topological surface state in Bi<sub>2</sub>Se<sub>3</sub>. A similar expelling of the surface state into bulk has been reported for SmB<sub>6</sub> upon ion irradiation [22].

Furthermore, in SmB<sub>6</sub> it was found that depending on the surface termination, the surface in-gap states are formed differently and consist mainly of the Sm 4*f* states, which indicates the importance of Sm 4*f* electrons for describing the surface states [23]. Using ionic liquid gating, it was possible to alter the surface state by modulating its conductivity by as much as 25% [24]. Furthermore, an alternative topologically trivial origin of the surface states due to a surface shift of the Sm 4*f* many-body resonance near the Fermi level was also proposed recently [25]. Recalling the valence instability and the ionic character of the Sm-B bond, it was also suggested that the polarity of the surface should have a strong effect on the formation and the type of the surface states [26].

Since even for a Sm compound with an integer bulk valency a shift of surface valency is not an unusual phenomenon [27], it is not surprising that evidence for a modified surface valency in SmB<sub>6</sub> and metallic Sm was revealed as early as 1980 [2]. In one of the most recent x-ray absorption studies, the surface

\*volodymyr.zabolotnyy@physik.uni-wuerzburg.de

†Present address: Max Planck Institute for Solid State Research Stuttgart, Heisenbergstraße 1, 70569 Stuttgart, Germany.

was reported [28] to consist almost entirely of  $\text{Sm}^{3+}$ . However, the direction in which the Sm oxidation shifts as compared to the average bulk value is not always universal [29,30]. For example, the opposite oxidation shift has been revealed on the surface of  $\text{SmOs}_4\text{Sb}_{12}$ . Similarly, a  $\text{Sm}^{2+}$ -enriched surface was reported for  $\text{SmB}_6$ , though only for Sm-terminated (001) regions [31].

In this context, a valuable insight is provided by scanning tunneling microscopy (STM) and spectroscopy (STS), as these methods offer detailed topographical maps [32] for a cleaved surface, and they detect the presence of reconstructions [33] or corrugations [34], as well as in-plane electronic inhomogeneities [32]. However, surface phenomena, including variations of the average Sm valence and the occurrence of surface states, are not solely bound to the topmost atomic layer. For example, a small enhancement in static magnetic fields on the scale of 40–90 nm was found in a recent muon-spin-relaxation experiment [35]. To study the depth-dependent valency on the nanometer scale, one may perform photoemission experiments at different take-off angles, thus modulating the average escape depth and hence the effective probing depth. Indeed, up to three different layers were reported at the cleaved  $\text{SmB}_6$  surface in a recent photoemission study [36]. However, uncertainties in the universal inelastic mean-free path of the photoelectrons caused by such effects as channeling may introduce considerable errors [37,38], so a more direct method is necessary.

Resonant soft x-ray reflectometry (RXR), combined with x-ray absorption spectroscopy (XAS), is such a method, which we use here to investigate the cleaved (001) surface of  $\text{SmB}_6$ . This nondestructive approach allows us to assess the chemical and valence profiles of flat samples on the length scale from a fraction to few hundreds of nanometers [39,40].

The paper is organized as follows: In Sec. II, we describe the sample preparation and experimental conditions, under which the reflectometry, absorption, and photoemission data were collected. In Sec. III, it is shown that the *in situ* prepared (100) sample surface is clean and remains stable during the data collection, without detectable absorption or desorption of residual gases, or any gradual loss of Sm or B atoms. In Sec. IV, we examine x-ray absorption spectra collected in the total electron yield (TEY) mode, which are commonly used to approximate the energy-dependent x-ray absorption cross section  $\sigma(E)$ . We also show that within 0.3% accuracy there are only two types of Sm ions contributing to absorption spectra. In Sec. V we introduce a crystal-field model, with which we fit our absorption data. Later in Sec. VI the model is refined and used to establish chemical density profiles for all atomic species with their respective valencies, including separate profiles for  $\text{Sm}^{2+}$  and  $\text{Sm}^{3+}$ . Finally, the results are discussed and compared to low-temperature photoemission in Sec. VII and summarized in Sec. VIII.

## II. METHOD AND SAMPLE PREPARATION

X-ray absorption and reflectivity measurements were performed using the four-circle UHV diffractometer at the REIXS 10ID-2 beamline of the Canadian Light Source in Saskatoon [41].

$\text{SmB}_6$  single crystals were prepared by the floating zone method as described elsewhere [42]. The crystals were

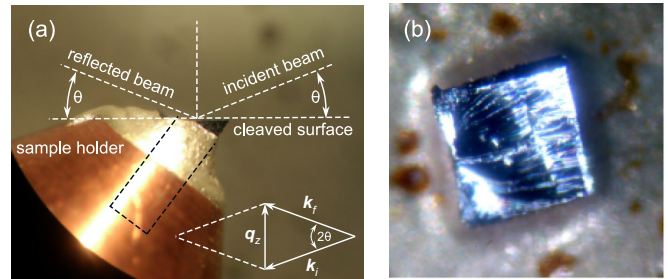


FIG. 1. (a) Experimental geometry. (b) Optical microscopy of the cleaved sample surface. The sample cross section is  $1 \times 1 \text{ mm}^2$ .

preoriented by Laue diffraction and cut in the form of long rods, which were then glued into conical holders (Fig. 1) and cleaved at room temperature in the fast-entry chamber at a pressure of  $10^{-8}$  mbar. Immediately thereafter, without breaking the vacuum, the samples were transferred into the measurement chamber of the diffractometer operated under UHV conditions, with a base pressure of better than  $2 \times 10^{-10}$  mbar. After two hours of alignment, the actual data were collected, starting with the sample stability and aging tests.

It was found that irrespective of the preorientation and the appropriate cutting, our samples cleaved such as to expose the (001) plane, which was confirmed by observation of the (001) Bragg peak in the reflectivity spectra. The most comprehensive and complete data set collected on one of these cleaves is presented and analyzed in this work.

Since synchrotron-based methods, such as photoelectron spectroscopy or x-ray reflectivity, are sensitive to comparatively large features reaching in size up to the beam cross section ( $\sim 100 \times 100 \mu\text{m}$ ), in Fig. 1(b) we show a typical microphotograph of a cleaved sample. Although the surface is not ideally flat, it consists of extended flat terraces, thus making specular reflectivity possible.

The soft x-ray photoemission data were collected on single crystals grown in Al-flux [43]. The Sm  $4f$  spectra were measured in the fixed mode of a VG Scienta R8000 electron analyzer at the MERLIN Beam line 4.0.3 at the Advanced Light Source (Berkeley, USA) with the photon energy of 70 eV. The B  $1s$  spectra were measured also in the fixed mode of a VG Scienta EW4000 analyzer at the I09 beamline of the Diamond Light Source (Didcot, United Kingdom) with the photon energy of 300 eV. The energy resolutions at both photon energies were better than 100 meV.

## III. SAMPLE STABILITY AND AGING

Sample aging is an especially notorious issue in photoemission [44], where just a fraction of a monolayer of residual gases adsorbed at the surface may critically change the low-energy spectrum by shifting the Fermi level via chemical doping, and/or by wiping out the  $k$  resolution due to the disrupted in-plane long-range atomic order [45]. In addition, a chemical shift may affect the core-level spectra [36].

X-ray reflectivity is typically not hindered by a few-nanometer-thick capping layer deposited either intentionally or as an unintended contamination that can be taken into account when modeling the RXR data. Nonetheless, a progressively

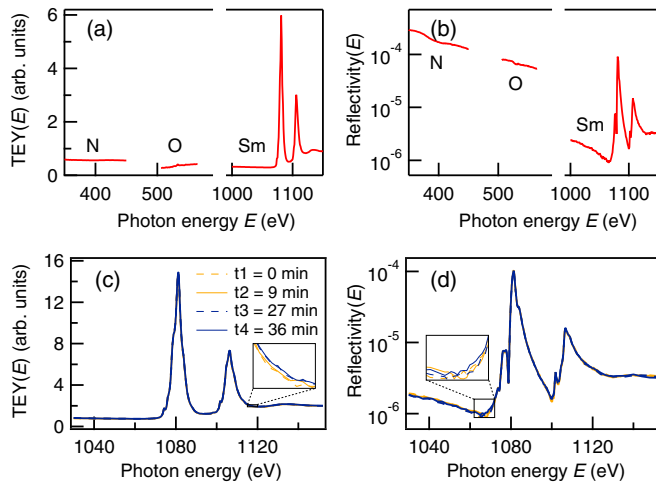


FIG. 2. (a), (b) TEY (absorption) and reflectivity spectra over the nitrogen  $K$  edge and oxygen  $K$  edge and samarium  $M_{4,5}$  edges. Sm spectra show sharp resonances due to  $3d \rightarrow 4f$  excitations [54]. (c), (d) Stability of the spectra in TEY and reflectivity modes. The four curves overlap nearly perfectly so that they can hardly be distinguished when overlaid.

growing or shrinking surface contamination layer would result in a drifting x-ray interference pattern, which in turn would render a set of measured spectra mutually inconsistent and impede the subsequent extraction of chemical profiles. This is especially true for samples introduced into the measuring chamber from ambient air due to desorption of CO or other volatile organic products from the solid surface [46–49]. Also samples, where the beam changes the stoichiometry at the surface [50,51], for example via light-induced oxygen vacancies [52], may pose a problem in this regard. The recently reported thermal desorption of Yb in  $\text{YbB}_{12}$  is just another specific example for a compositional surface instability [53]. The aforementioned problems may partly be seen not only in reflectivity, but also in absorption spectra, which undergo a strong drift on the timescale of several hours [30]. The prevention of these problems was one of the main incentives behind resorting to a more involved *in situ* surface preparation.

To check whether the *in situ* cleavage solves the problem, in Figs. 2(a) and 2(b) we compare the TEY and RXR spectra measured over the absorption edges of the dominant residual gases in our fast-entry chamber to the  $M_{4,5}$  absorption edge of Sm used as a scale. As one can see, the spectra at the oxygen and nitrogen  $K$  edges are practically flat, signifying virtually no surface contamination.

Although the data presented in Figs. 2(a) and 2(b) exclude any substantial surface contamination that may start gradually desorbing under the x-ray beam, there still remains a risk that the beam affects Sm and B compositions at the surface. To test if this is of any relevance for the *in situ* cleaved  $\text{SmB}_6$ , we measured one and the same spectrum several times in a row: first, two sequential spectra collected with nominal beam intensity; then a so-called “burning” spectrum measured with about  $20\times$  higher beam intensity; and again two spectra with nominal intensity. The four nominal spectra are shown in Figs. 2(c) and 2(d). Again, up to small random variations due to statistical noise, all the spectra are found to be identical. Thus,

we conclude that neither desorption of surface contaminants nor drift in stoichiometry are an issue, and the sample remains stable over the time of data collection.

#### IV. DECOMPOSING SAMARIUM TEY SPECTRA

$\text{SmB}_6$  is a mixed-valency system [1–11], therefore generally we expect an absorption spectrum to be the sum of two different components [56] corresponding to  $\text{Sm}^{2+}$  and  $\text{Sm}^{3+}$  ions, respectively. However, in the case of a substantial inhomogeneity, the number of different components may be larger. For example, at a predominantly Sm-terminated surface, there could be a considerable number of Sm atoms with changed coordination number as compared to the bulk, hence each individual TEY spectrum would become a weighted sum of three, or maybe more, components: two corresponding to the bulk  $\text{Sm}^{2+}$  and  $\text{Sm}^{3+}$  while others representing the Sm ions with disrupted coordination or oxidation state:

$$S(\omega) = \alpha_1 C^1(\omega) + \alpha_2 C^2(\omega) + \alpha_3 C^3(\omega) + \dots \quad (1)$$

The intuition here is that a change in the incidence angle and/or the polarization of the x rays would affect the weighting coefficients  $\alpha_i$  so that upon recording a set of spectra  $\{S_n(\omega)\}$  with varying contributions of the components  $C_i(\omega)$ , we can eventually find the components themselves, or at least their number, that is the dimensionality of the basis in which each of the measured spectra can be expanded. Obviously, the basis formed by the component spectra  $\{C_i(\omega)\}$  is not unique. However, applying singular value decomposition (SVD), one can objectively determine the minimal number of *significant* components that are relevant at a given quality of the input data. SVD is a very powerful method used in the analysis of magnetic resonance imaging [57] and other biological data [58], NEXAFS microscopy, and resonant scattering [59].

Suppose that we have  $N$  absorption spectra with  $M > N$  points, each measured on the same energy grid  $\{\omega_m\}$ ,  $m = 1, \dots, M$ , under progressively changing conditions. The measured data can be placed in a  $M \times N$  matrix, such that each column contains a particular spectrum. We can always perform SVD decomposition of this matrix, in which we represent  $S$  as

$$S_{M \times N} = U_{M \times M} W_{M \times N} V_{N \times N}^T, \quad (2)$$

were  $U$  and  $V$  are orthogonal matrices and  $W = (w_{i,j}) = (\lambda_i \delta_{i,j})$  is the diagonal matrix, containing the singular values  $\lambda_i$  in decreasing order. If the measured spectra are linear combinations of only  $p$  components, then only the first  $p$  singular values will be nonvanishing, i.e., all spectra can be expanded in the first  $p$  columns of the matrix  $U$ . Since real spectra also contain statistical noise, the value of the remaining singular values will be determined by the noise level, and for a purely random matrix the singular values  $\lambda_k$  will follow the so-called Marchenko-Pastur distribution [60], exhibiting a close-to-exponential decrease with  $k$ . Although we cannot exclude the presence of extremely weak components swamped by the noise, the approach allows us to draw an objective demarcation line between those components whose singular values are above the noise bed and those that can be discarded as unjustified by the current signal-to-noise ratio [61].

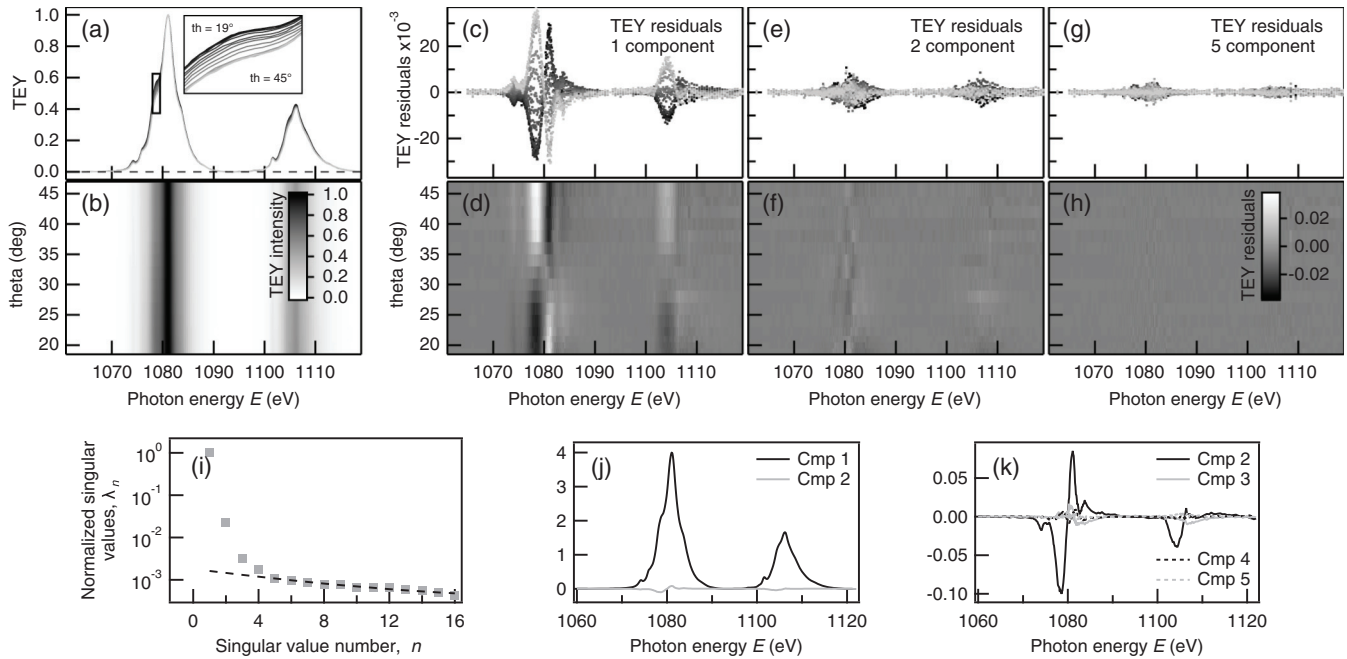


FIG. 3. SVD decomposition of the TEY data. (a), (b) TEY spectra after subtraction of Shirley-type background [55] and normalization of the peak intensity to one. The false-color plots duplicate the data presented in the line plots and elucidate the trends in the  $\theta$ -energy parameter space in a more convenient way. Panels (c)–(h) show residuals for one-, two-, and five-component representations. (i) Normalized singular values in decreasing order. (j), (k) The first five most significant components.

It is also worth mentioning that regardless of the actual reasons, considering only the first  $p$  singular values provides the best mean-squares  $p$ -component fit to the original data, which is the essence of the Eckart-Young theorem [62].

In Fig. 3 we present the results of an application of the SVD analysis to a set of TEY spectra measured with  $\sigma$ -polarized light for  $\theta$  ranging from  $18^\circ$  to  $45^\circ$ . As can be seen in Figs. 3(c) and 3(d), there remains a clear structure in the residuals with the errors amounting up to 3%; therefore, a single component is clearly not enough to describe the data. Increasing the number of components to two [Figs. 3(e) and 3(f)] results in an almost perfect description of the experimental data, with very little residual structure discernible beneath the noise. This means (i) the experimental data can essentially be expanded in two basis spectra and (ii) the overall variation between individual spectra relative to the averaged one is unfavorably small, of the order of  $\lambda_2/\lambda_1 = 0.023$ , though still much larger than the noise level, which is given here by  $\lambda_5/\lambda_1 \sim 10^{-3}$ .

From the plot of the singular values [Fig. 3(i)] we can actually discern four different components that still stand out above the noise bed marked by the dashed line. Recalling that TEY spectra are often distorted by self-absorption effects [63–66], one may try to explain the two “unwanted” components out by arguing that the self-absorption would break down the linearity assumptions [67,68] on which our SVD analysis is based. This is indeed a valid argument, however, nonlinearity would produce deviations that monotonically change as the total intensity grows with  $\theta$ , so we would observe largely positive residuals on one side of some optimal  $\theta_0$  and largely negative residuals on the other side. Since this is not the case [see Fig. 3(f)], there indeed must be at least four different components in the data set, presumably due to slightly different effective crystal fields experienced by  $\text{Sm}^{2+}$  and  $\text{Sm}^{3+}$  at the

surface and bulk, respectively. Since components number 3 and 4 are very weak as compared to components number 1 and 2 (with ratios  $\lambda_3/\lambda_1 \sim 3 \times 10^{-3}$ ,  $\lambda_4/\lambda_1 \sim 2 \times 10^{-3}$ ) and to the noise, we can safely disregard them. In Figs. 3(j) and 3(k), we plot the first five components  $C^k(\omega_n) = \lambda_k v_{n,k}$ ,  $k = 1, \dots, 5$ .

Thus, from the SVD decomposition we can justly conclude that only two components are major contributors to the measured spectra and that the relative gross error, due to discarding other components, as well as due to self-absorption effects is of the order of 0.3%. We should also emphasize that  $C^1(\omega_n)$ ,  $C^2(\omega_n)$  are not the  $\text{Sm}^{2+}$  and  $\text{Sm}^{3+}$  spectra themselves, but some linear combinations of these. Generally,  $C^1(\omega_n)$  represents common features among the processed spectra, while further components,  $C^2(\omega_n)$ ,  $C^3(\omega_n)$ ,  $\dots$  elucidate the differences in the decreasing order.

To find the  $\text{Sm}^{2+}$  and  $\text{Sm}^{3+}$  spectra, one may try to include some additional restrictions/assumptions, like non-negativity [58], known branching ratio between the spin-orbit split multiplets [69,70], etc. In this particular case, we will, however, rely on the crystal-field theory (CFT) calculation as a source of restrictions, whereas the physical parameters, like Coulomb repulsion and transition lifetimes, will be treated as unknown fit parameters to be obtained from experiment.

## V. $M_{4,5}$ EDGE, FIT TO CRYSTAL-FIELD CALCULATIONS

In this section we introduce a minimal Hamiltonian that is sufficient to model the  $M_{4,5}$  resonant absorption edge of the Sm ions and fit the model to the experimental absorption represented by TEY spectra.

Hybridization between the  $f$  subsystem and the rest of the conduction electrons in  $\text{SmB}_6$  is an important interaction responsible for the development of the coherent Kondo state

at low temperatures [71,72]. The effect of this hybridization is estimated to be of the order  $V_{kf}/U_{df}$  [73], where the coupling between the valence and  $f$  electrons,  $V_{kf} \sim 1$  eV, is much smaller than the Coulomb interaction  $U_{df} \sim 10$  eV. Therefore, we neglect the hybridization and use a single-ion model that includes 14  $f$  and 10  $d$  orbitals, which also would be the minimal orbital set to describe  $3d \rightarrow 4f$  resonant excitations.

Considering the three major interactions, i.e., Coulomb contribution, spin-orbit coupling, and crystal-field effects, the Hamiltonian can be written as [74]

$$\hat{H} = \hat{H}_{\text{Coul}} + \hat{H}_{\text{SO}} + \hat{H}_{\text{CF}}. \quad (3)$$

The Coulomb part

$$\hat{H}_{\text{Coul}} = \frac{1}{2} \sum_{mm'm''m'''} U_{mm'm''m'''} \hat{c}_m^\dagger \hat{c}_{m'}^\dagger \hat{c}_{m''} \hat{c}_{m'''}, \quad (4)$$

responsible for the electronic correlations and the resulting multiplet structure, is the most significant contributor. In our model, we fully account for the  $f$ - $f$  and  $f$ - $d$  interactions. For example, the  $f$ - $f$  contribution ( $l = 3$ ) has the following form:

$$U_{mm'm''m'''}^{ff} = \sum_{k=0}^l a_k(m, m', m'', m''') F_{ff}^{(2k)}, \quad (5)$$

where all  $a_k$  are known coefficients specific to the set of the  $f$  orbitals so that  $U^{ff}$  is fully determined by the four Slater integrals  $F_{ff}^{(0)}$ ,  $F_{ff}^{(2)}$ ,  $F_{ff}^{(4)}$ ,  $F_{ff}^{(6)}$ . The integrals themselves can be estimated from the radial part of the  $f$  orbitals [75] and, if necessary, later refined by fitting to experimental data. It is noteworthy that the  $F_{ff}^{(0)}$  integral usually cannot be determined reliably due to the screening by the conduction electrons [76]. Since the  $F_{ff}^{(0)}$  results in the rigid shift of absorption spectrum as a whole, which will be anyway fitted here, this theoretical challenge does not entail any practical consequence for the current consideration. In a similar way, the  $f$ - $d$  part depends on five other parameters, controlling so-called direct ( $F_{df}^{(2)}$ ,  $F_{df}^{(4)}$ ) and exchange ( $G_{df}^{(1)}$ ,  $G_{df}^{(3)}$ ,  $G_{df}^{(5)}$ ) Coulomb interactions between  $f$  and  $d$  orbitals [74].

Within the central field approximation, the spin-orbit interaction reduces to two constants  $\zeta_{3d}$  and  $\zeta_{4f}$ , determining the strength of the spin-orbit coupling in the  $d$  and  $f$  shells, respectively:

$$\hat{H}^{\text{SO}} = \zeta_{3d} \hat{\mathbf{L}}_{3d} \cdot \hat{\mathbf{S}}_{3d} + \zeta_{4f} \hat{\mathbf{L}}_{4f} \cdot \hat{\mathbf{S}}_{4f}. \quad (6)$$

In  $\text{SmB}_6$ , the central Sm ion is surrounded by eight B cages located in the vertices of a cube. This forms the source of a cubic crystal field (CF). Based on the spatial extent of the radial functions, we can order the total CF splitting of the  $3d$  core and  $4f$  valence levels as  $\Delta_{\text{CF}}(3d) \lesssim \Delta_{\text{CF}}(4f)$ , which suggests that the CF effects in the  $d$  shell can be safely neglected in Eq. (6), if the  $f$ -shell CF can be deemed negligible. Reliable values of the  $f$ -shell CF in  $\text{SmB}_6$  are hard to find. Only recently it has been firmly established that it is the fourfold-degenerate  $\Gamma_8$  multiplet that forms the ground state in the  $J = \frac{5}{2} f^1$  configuration [77]. However the magnitude of the CF can be

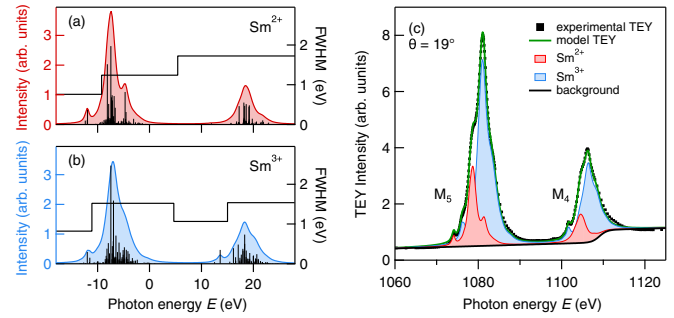


FIG. 4. (a), (b) CFT calculations for  $\text{Sm}^{2+}$  and  $\text{Sm}^{3+}$ . The spiky spectrum shows the transition energies and their probabilities, as they result from CFT calculation, whereas the continuous curves shows the lifetime-broadened spectra. The corresponding energy-dependent lifetime  $\Gamma(E)$  is plotted against the right axis. (c) Fit (green line) to the experimental TEY signal (black dots) with the weighted sum of the two Sm components and the smooth background due to the continuum excitations modeled as slope with broadened edges. Only  $M_5$  edge is within the plotted region.

inferred from the homologous compound  $\text{CeB}_6$ , where the CF splitting of the  $4f$  levels ( $\Gamma_8 - \Gamma_7$  splitting of  $J = \frac{5}{2} f^1$  configuration) has been determined experimentally to be of the order of 46 meV [78–80]. Lower values with a wider spread ranging from 1 to 27 meV were reported for the overall CF splitting of the  $4f$  levels in  $\text{SmB}_6$  [9,34,81,82]. Since the splitting of the energy levels caused by the CF is very small, in fact comparable to or smaller than the experimental energy resolution of our experimental data (100–200 meV), we omit the CF altogether, similar to other works [83]. We do so in order to avoid unnecessary numeric overhead, although the effective CF for the  $3d$  and  $4f$  electrons could have been easily included, were it necessary.

The resonant part of the absorption spectrum can thus be calculated up to a proportionality factor as

$$f_2^{\text{res}}(E) \sim \frac{1}{Z} \sum_{\alpha} e^{-\frac{E_{\alpha}}{k_B T}} \sum_{\beta} |(\Psi_{\beta}(\theta, \varphi) | \vec{\epsilon} \cdot \vec{r} | \Psi_{\alpha}(\theta, \varphi))|^2 \times \frac{-1}{\pi} \text{Im} \left[ \frac{1}{(E_{\beta} - E_{\alpha} - E) + i \frac{\Gamma(E)}{2}} \right]. \quad (7)$$

Here, the outer sum takes care of the thermodynamic averaging for a finite temperature  $T$ , including a possible degeneracy of the initial state  $|\Psi_{\alpha}\rangle$ . The inner sum accounts for the transition probabilities between the initial  $|\Psi_{\alpha}\rangle$  and the final  $|\Psi_{\beta}\rangle$  states, whereas the corresponding lifetimes are given by the function  $\Gamma(E)$ , which in the current consideration is to be determined from fits to experimental data. The polarization of the incident radiation is given by  $\vec{\epsilon}$ .

To perform the actual calculation we used the QUANTY [84–88] framework developed by Haverkort, which offers a convenient and flexible way to program this quantum mechanical problem in second quantization. The calculated spectra and the optimized input constants are shown in Fig. 4 and Table I. As evident from the table, unlike Ref. [89], we use two separate sets of Slater  $F_{ff}^{(k)}$  integrals and the spin-orbit coupling  $\zeta_{4f}$ . The reason for this is the relaxation of atomic orbitals upon

TABLE I. Optimized CFT parameters for  $\text{Sm}^{2+}$  and  $\text{Sm}^{3+}$  ions.

Ion	State	Configuration	$F_{ff}^{(2)}$	$F_{ff}^{(4)}$	$F_{ff}^{(6)}$	$\zeta_{4f}$	$F_{df}^{(2)}$	$F_{df}^{(4)}$	$G_{df}^{(1)}$	$G_{df}^{(3)}$	$G_{df}^{(5)}$	$\zeta_{3d}$
$\text{Sm}^{2+}$	Initial	$3d^{10}4f^6$	10.828	6.751	4.845	0.136						
	Final	$3d^9 4f^7$	11.548	7.218	5.185	0.165	6.701	3.075	4.670	2.734	1.888	10.514
$\text{Sm}^{3+}$	Initial	$3d^{10}4f^5$	10.950	6.873	4.945	0.152						
	Final	$3d^9 4f^6$	11.548	7.260	5.227	0.180	7.211	3.337	5.086	2.979	2.058	10.510

the  $3d \rightarrow 4f$  excitation, accounting for which should improve the match between our model and the experiment.

Figures 4(a) and 4(b) show the spectra as calculated by the QUANTY code and broadened according to the energy-dependent lifetime  $\Gamma(E)$ , plotted against the right axis. Figure 4(c) demonstrates the actual match to the experimental TEY data, in which the TEY is modeled as a sum of the  $3+$  and  $2+$  components and a smooth background due to the continuum excitations.

As can be seen, the calculated model curves fit well to the experimental data, while the optimized values of the Slater integrals are not much different from those reported in an earlier *ab initio* calculation [54,89]. Importantly, we also find that the parameters quoted in Table I nicely reproduce properties of the ground-state spectrum, namely, the transition energies  $\Delta E(^7F_0 \rightarrow ^7F_1) = 40$  meV in  $\text{Sm}^{2+}$  and  $\Delta E(^6H_{5/2} \rightarrow ^6H_{7/2}) = 120$  meV in  $\text{Sm}^{3+}$ , as measured by inelastic neutron scattering experiments [9,90,91]. Therefore, the constructed model can be considered as a good approximation to the resonant absorption of  $\text{Sm}^{2+}$  and  $\text{Sm}^{3+}$  ions. This is further validated by taking into account that TEY data exhibited little evidence for nonlinearity, and as a consequence, for the saturation and self-absorption effects that could have drawn the TEY signal away from the “true” absorption.

The overall angular dependence of the TEY signal is sufficiently involved to merit a separate consideration [92–94]. To circumvent these difficulties in the next section, we use instead x-ray reflectometry, which in addition to chemical and valence profiles allows for extraction of atomic scattering factors in absolute units.

## VI. CHEMICAL AND VALENCE PROFILING USING X-RAY REFLECTOMETRY

To obtain chemical profiles  $c_i(z)$  for all of the atomic species  $i$  composing the sample and to further refine the on-resonance atomic scattering factors of  $\text{Sm}^{2+}$  and  $\text{Sm}^{3+}$ , we use resonant x-ray reflectometry [39,40], which is an element and bulk-sensitive technique, that previously proved to be useful in determining chemical composition, valence and magnetization profiles, orbital ordering [95–99], and very recently was used to extract information about the electronic properties of oxide heterostructures [70].

The method relies on the fact that for a flat-layered sample, the intensity of the specularly reflected x-ray beam  $R(q_z, E)$  can be relatively easily obtained from the position- and energy-dependent complex refractive index  $n(z, E)$ , which in turn is given by the sum of the contributions of all the atoms

composing the material [95,100]

$$n(z, E) = 1 - \frac{r_e \lambda^2}{2\pi} \sum_i c_i(z) f_i(E). \quad (8)$$

Here,  $r_e$  is the classical electron radius,  $\lambda$  is the wavelength of the exciting radiation,  $c_i(z)$  is the spatially varying atomic concentration for the atomic species  $i$ , and  $f_i(E)$  is the corresponding total complex atomic scattering factor. The  $z$  axis is aligned perpendicularly to the sample surface, while the sample is assumed to be homogeneous in the  $x$ - $y$  plane.

The generic approach to analyze reflectometry data  $R^{\text{expt}}(q_z, E)$  is to parametrize both the chemical profiles  $c_i(z)$  and the atomic scattering factors  $f_i(E)$ , with models appropriate to the problem at hand, and then to optimize all unknown parameters so that the reflectivity  $R^{\text{mod}}(q_z, E)$ , modeled based on  $c_i(z)$  and  $f_i(E)$ , fits the experimentally measured spectra  $R^{\text{expt}}(q_z, E)$ . To perform this task, we combine the Parratt formalism [102] with a differential evolution for optimization of the fit parameters [95,103,104]. We parametrize the continuous chemical profiles  $c_i(z)$  by a set of layers  $l = 1, 2, \dots, N$  with certain thicknesses  $d_{i,l}$ , concentrations  $c_{i,l}$ , and roughnesses  $\sigma_{i,l}$  [95]. The latter determine how rapidly the concentration changes between neighboring layers.

First, we pin down the parameters driving the concentration profiles. For this, we use  $\theta$ - $2\theta$  scans measured at constant energies ranging from  $E = 375$  eV up to 1200 eV. At this stage, we rely on the off-resonant energies, for which we can utilize theoretical scattering factors provided by Chantler [101]. Analyzing the experimental data, it turned out that  $N = 4$  layers were already enough to build a sufficiently detailed representation of  $c_i(z)$ . The atomic concentrations  $c_{\text{B},1}$  and  $c_{\text{Sm},1}$  for the deepest layer  $l = 1$  were kept fixed at their stoichiometric values calculated from the known bulk crystal structure [105,106]. Parameters for the remaining three layers were treated as unknown and were determined from the fits. At this stage, we did not discriminate between  $\text{Sm}^{2+}$  and  $\text{Sm}^{3+}$  yet, instead one common atomic concentration  $c_{\text{Sm},l} = c_{\text{Sm}^{2+},l} + c_{\text{Sm}^{3+},l}$  was used.

In x-ray reflectometry, to distinguish between different atomic species, the atoms have to differ in their scattering factors  $f_i(E)$ , due to different oxidation states, different crystal field, or any other reason. That is why away from the resonance energies,  $\text{Sm}^{2+}$  and  $\text{Sm}^{3+}$  remain essentially indistinguishable. Therefore, in order to establish separate valence profiles,  $c_{\text{Sm}^{2+},l}$  and  $c_{\text{Sm}^{3+},l}$ , one has to move into the resonance energy range shown in Fig. 4. As one may see,  $\text{Sm}^{2+}$  and  $\text{Sm}^{3+}$  slightly differ in position and form of the resonance peaks, which eventually allows separate valence profiles to be extracted from the reflectometry data. Again, like at the first stage, we fix the concentrations of the Sm atoms located in the bulk layer, such

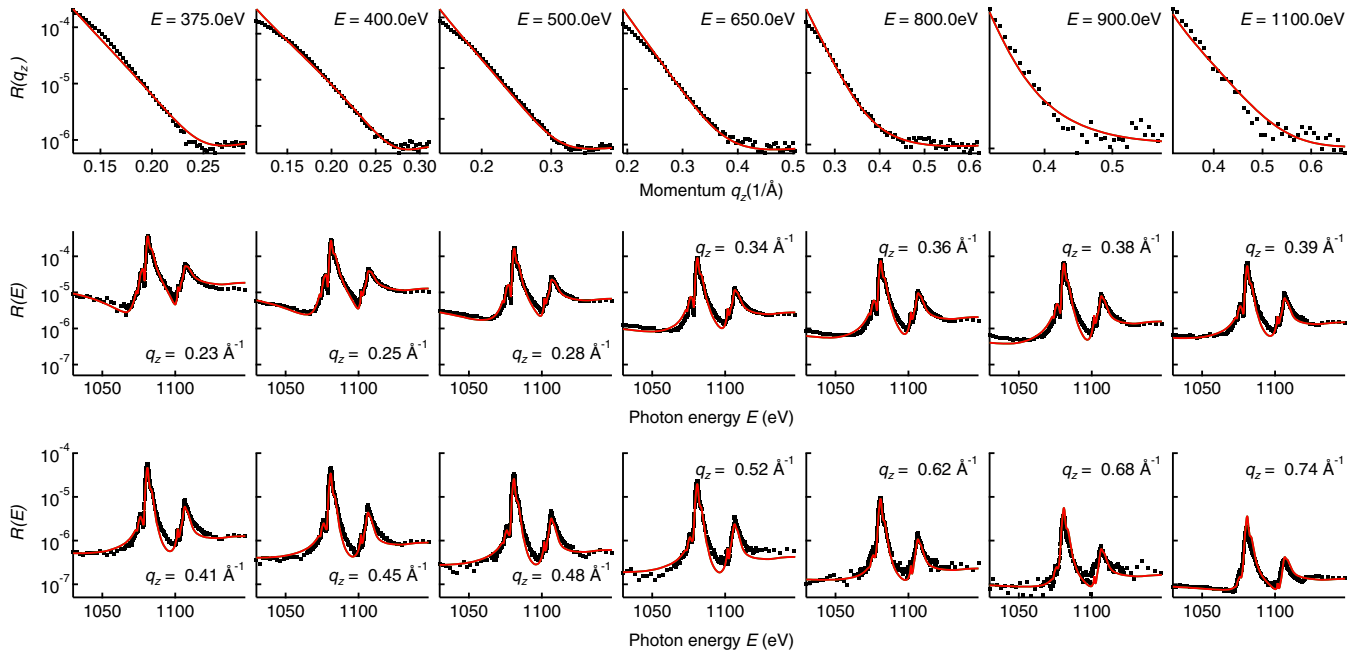


FIG. 5. Fits to reflectivity data, measured as off-resonant momentum scans (upper row) or on-resonance (lower two rows) energy scans. The red curves correspond to the calculated reflectivity  $R^{\text{mod}}(q_z, E)$ , while the black symbols show the experimentally measured intensity  $R^{\text{exp}}(q_z, E)$ . Here, we show representative spectra out of those used in the actual fit so that all energies and momentum transfers are uniformly covered.

that the average valency matches the value of +2.56, known from literature [107–111]. For the remaining layers, all their parameters are treated as unknown fit variables.

The total scattering factor in this region is taken as the sum of the off-resonant part, as provided by Chantler [101], and the resonance part as derived in Sec. V based on CF calculations with the real part of the scattering factor determined via Kramers-Kronig transformation [112].

In addition to the unknown scaling and energy offset in the resonance part, we also allow for a small energy shift and broadening in the steplike off-resonance part.

As the last stage, we let all the unknown fit parameters relax completely by optimizing the chemical composition profile and the on-resonance optical constants simultaneously. The

resulting fits to reflectivity data are shown in Fig. 5, whereas the chemical profiles, together with the atomic scattering factors for  $\text{Sm}^{2+}$  and  $\text{Sm}^{3+}$ , are provided in Fig. 6.

### VII. DISCUSSION AND COMPARISON TO PHOTOEMISSION

Aside from the stoichiometric bulk, we can single out three different layers at the surface of the cleaved sample, each approximately one to two unit cells thick. Counting from the bulk (B) on the left (see Fig. 6) these are as follows: (i) A region with a mild prevalence of  $\text{Sm}^{3+}$  over  $\text{Sm}^{2+}$  and a slight boron deficiency. (ii) In the second region, the boron deficiency continues to increase, but the major feature here is the almost

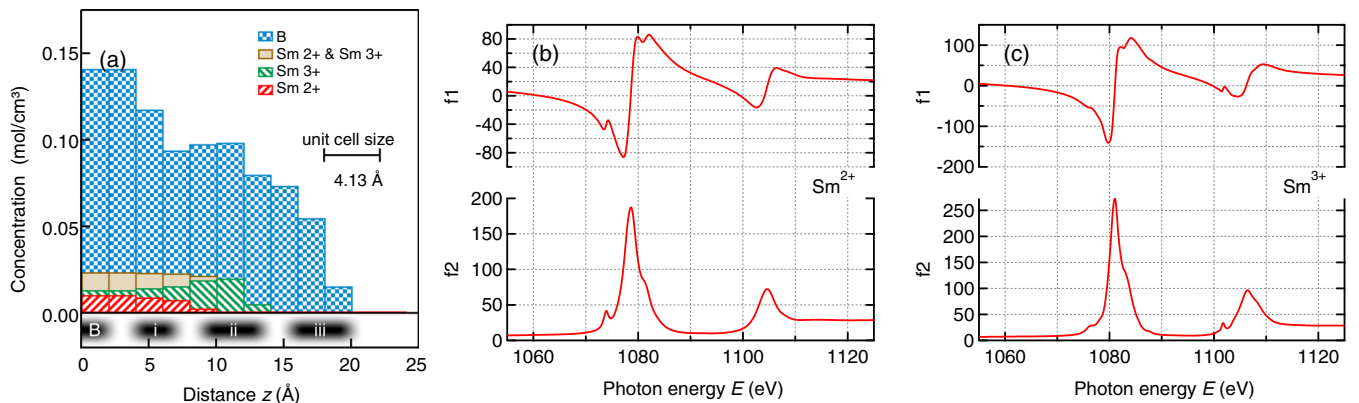


FIG. 6. (a) Chemical and valence profiles  $c_i(z)$ , resulting from reflectivity fits presented in Fig. 5. “Sm2+ & Sm3+” is the sum of  $\text{Sm}^{2+}$  and  $\text{Sm}^{3+}$  components, i.e., the total Sm content regardless of the valency. (b), (c) The atomic scattering factors necessary for calculation of the refractive index  $n(z, E)$ . The factors were taken from Chantler [101], except for the Sm on-resonance region, which derives from the previous Sec. V and was further optimized to reflectivity data.

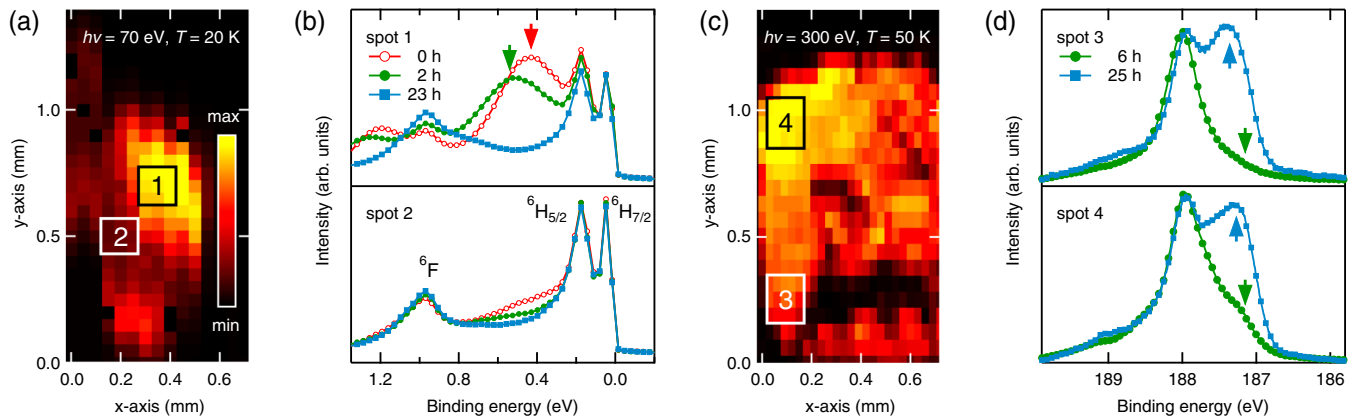


FIG. 7. (a) Variation of the photoemission intensity over the cleaved surface, measured at the binding energy of the Sm  $4f$  surface peak ( $E_{\text{Bind}} \sim 0.5$  eV). Based on this intensity map, one can define regions with initially high (spot 1, black square) and low (spot 2, white square) Sm surface signal. (b) Time evolution of the Sm  $4f$  surface peak averaged over the spot 1 and spot 2. The plotted energy range covers the  ${}^6\text{F}$  and  ${}^6\text{H}$   $\text{Sm}^{2+}$  final-state multiplets, while the  $\text{Sm}^{3+}$  multiplets are found at higher binding energies [31,114]. (c) Intensity map at the B  $1s$  surface peak ( $E_{\text{Bind}} \sim 187.3$  eV). (d) Corresponding time evolution for the regions with initially low B  $1s$  surface contribution (spot 3) and high contribution (spot 4). The energy position of the respective surface peaks is denoted by the vertical arrows. As time passes on, the inhomogeneity vanishes, both in terms of Sm  $4f$  and B  $1s$  surface contributions.

complete prevalence of  $\text{Sm}^{3+}$ . (iii) The last and outermost region appears to be containing only boron atoms with trace amounts of Sm. The absence of any substantial quantities of Sm atoms at the very surface is also corroborated by our analysis of the TEY data, as otherwise Sm atoms with broken cubic crystal field should have appeared as additional components in the SVD decomposition of the surface-sensitive TEY data.

In the following, we discuss how the extracted chemical and valence profiles relate to the microscopic structure of the cleaved surface. Had the cleavage occurred primarily between the Sm and  $\text{B}_6$  layers, *without any considerable loss* of B or Sm atoms, as reported by the most of the low-temperature STM studies, then the observation of a B-rich surface would seem quite strange. In contrast to these low-temperature data, our finding of a boron-rich surface appears to be compatible with the high-temperature STM [113], where the most probable cleavage plane was concluded to cut through the  $\text{B}_6$  octahedra so that both counterparts would be B terminated upon crystal fracture. A preferably B-terminated surface was also reported for low-temperature cleaved  $\text{SmB}_6$  in a photoemission study [114], but the nonstoichiometry at the surface was found to be so profound that possible loss of Sm had to be conjectured. Both loss of Sm and a boron-rich surface were also reported for an electron-beam annealed  $\text{SmB}_6$  (001) surface [115], suggesting some level of uniformity in experimental observations. However, in the most recent photoemission study [36], it was possible to select differently terminated surface spots using an x-ray beam of a few hundred microns in diameter, which implies that microscopic lateral inhomogeneities may play an important role at a cleaved surface of  $\text{SmB}_6$ .

Unlike STM, both photoemission and x-ray reflectivity are laterally averaging techniques on a similar length scale of  $\sim 100$   $\mu\text{m}$ . Considering this similarity, it is insightful to make a closer comparison of the two experimental methods. Here, we perform such a comparison to Al-flux grown  $\text{SmB}_6$  single crystals cleaved and held in UHV conditions at  $T \leq 50$  K. It is notable that right after the cleavage, one can

clearly distinguish between Sm- and B-terminated regions in photoemission signal, though on the time scale of 6–24 h the difference gradually fades away and the surface becomes homogeneous with the boron B  $1s$  states as the only significant surface-related feature. In Fig. 7 we illustrate this evolution by tracing the Sm  $4f$  valence [Figs. 7(a) and 7(b)] and B  $1s$  core [Figs. 7(c) and 7(d)] levels measured with soft x rays. Aside from the sharp bulklike peaks, broad surface peaks appear as shoulders at a lower binding energy for B  $1s$  and at a higher binding energy for Sm  $4f$  states. As shown by Denlinger *et al.*, the Sm surface feature originates from broadened and shifted versions of the  $\text{Sm}^{2+}$  final-state multiplets [31].

These surface peaks allow us to tag different surface regions as being nominally boron or samarium terminated [31]. The surface peaks exhibit a clear dependence on time, in general reducing their intensity with the time passed after the cleavage. More precisely, at the Sm-terminated area, we observe a reduction of the Sm surface peak, accompanied by a gradual development of the surface boron peak. The boron-terminated area shows a comparable progressive development in the surface boron peak, while the Sm surface feature is almost absent. After 23 h aging at low temperature the spectra from the two initially different regions become very similar: boron spectra develop a surface-related shoulder at the B  $1s$  peak, but Sm  $4f$  spectra show no significant traces of the surface peak [Figs. 7(b) and 7(d)].

In its outline, this spectral development can be well understood in terms of Sm loss, as originally conjectured by Aono *et al.* [115]. In Fig. 8 we *schematically* illustrate the process and the resulting chemical profiles. It is equally probable to obtain either Sm- or B-terminated patches upon the sample cleavage. Therefore, if probed selectively in the photoemission experiment, the Sm-terminated patches will initially exhibit a notable surface-related Sm peak, while the B-terminated patches, a boron surface peak. As time passes on, the surface Sm atoms are gradually lost and the Sm surface peak vanishes. The lack of these atoms will disrupt the underlying boron layer,

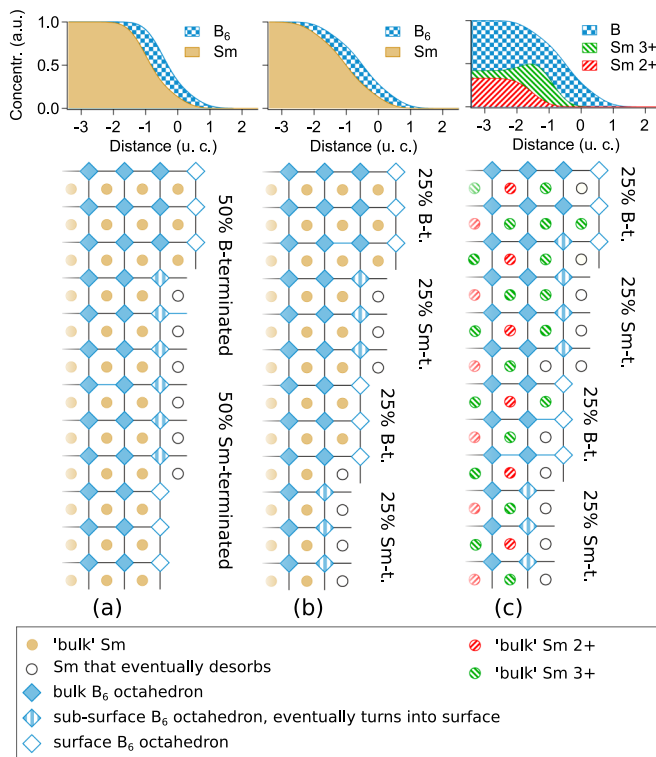


FIG. 8. Schematic representation of a cleaved surface of  $\text{SmB}_6$  and the resulting laterally averaged chemical profiles of the aged sample, a state attained upon loss of surface Sm atoms (shown as open circles). (a) The simplest case. (b) An elaboration of the schematic model via inclusion of surface steppiness or roughness. (c) Further elaboration of the qualitative model with separate representation of  $\text{Sm}^{2+}/\text{Sm}^{3+}$  ions and a deeper loss of Sm ions.

which in turn leads to the growth of the B surface peak at the former Sm patches. At the B-terminated patches, in contrast to the Sm patches, no such massive changes are expected. The reason for this lies in the relative stability of the boron sublattice and its protection of the topmost Sm layer.

Likewise, the loss of the Sm surface atoms is essential to understanding of the B profile, as extracted from the x-ray reflectometry data. Immediately upon cleavage, neither Sm nor B should protrude in the laterally averaged chemical profiles. But later, owing to the loss of Sm, an “aged” surface of  $\text{SmB}_6$  will eventually exhibit a B profile that extends beyond that of Sm. A schematic illustration for this can be found in Fig. 8(a). The schematics can be further improved to cover the less abrupt onset of boron, as seen in the experimental data [Fig. 6(a)]. For that, one has to account for the stepped character of the cleaved surface and a possible loss of some B atoms by the damaged surface  $\text{B}_{6-x}$  octahedra, as shown in Fig. 8(b). To facilitate the comparison to the reconstructed chemical profiles, in Fig. 8(c) we further elaborate our qualitative model by differentiating between  $\text{Sm}^{2+}$  and  $\text{Sm}^{3+}$  ions and by increasing the penetration depth of Sm vacancies beyond the topmost layer. As can be seen, there is a subsurface region of almost pure  $\text{Sm}^{3+}$  before the true bulk mixed valent state is recovered.

There is another important comparison to the photoemission data to be made. Namely, one has to clarify the apparent disparity of the time scales on which the surface reconstruction occurs. As shown in Sec. III, in the case of the room-

temperature reflectometry, the process must have been over by the end of the sample alignment, which provides the upper limit of 2 h for the reconstruction. On the other hand, in the case of the low-temperature photoemission, the reconstruction takes 6–24 h.

Although a deposition of residual gases could have been a big problem for the reflectometry analysis, it is unlikely to play an important role in the reconstruction since an accidental deterioration of vacuum does not seem to have any effect on the pace of the reconstruction [36]. As we see from our data, the process appears to be thermally activated, similarly to time-dependent Yb valence drift, observed in another photoemission study [116]. This key role of the temperature in the surface reconstruction offers a natural explanation to the differences between the low [32–34] and high [113] temperature STM measurements.

It is worth noting that the increased concentration of  $\text{Sm}^{3+}$  at the surface compares well with other experimental works. For example, in the recent  $\mu\text{SR}$  study Biswas *et al.* found an enhancement of static magnetic fields near the surface [35]. The finding was attributed to an increasing number of  $\text{Sm}^{3+}$  moments at the surface, which is complemented by this work.

To conclude this discussion, we want to remind that, partially due to the ease of preparation, this work was performed on a cleaved surface. These days, however, a well-ordered surface of  $\text{SmB}_6$  (001) can also be obtained by *in situ* sputtering and controlled annealing in UHV [117–119]. Such annealed surfaces exhibit metallic surface states, are well ordered over a wide area, and allow for a much finer control of surface stoichiometry. Based on the theoretical prediction about the energy position of the B  $2p$  surface feature [26] and the results of scanning tunneling spectroscopy [118] it was concluded that Sm-rich surface termination is achieved at low annealing temperatures ( $\approx 1080^\circ\text{C}$ ), while a B-rich surface results at high temperatures ( $> 1200^\circ\text{C}$ ).

One, however, should remember that the enrichment of the low sputtering component in the surface region [120] together with the accumulation of in-depth disorder and defects [121,122] such as vacancies and implanted atoms on a length scale of 3–100 nm may substantially modify the physical surface properties, such as the surface dielectric tensor [123] or the overall morphology [124]. Even topologically nontrivial surface states are not exempt from the influence of the surface disorder produced by ion sputtering. Introducing unitary disorder at the surface, Queiroz *et al.* were able to push the Dirac state inward into the quintuplet layers of  $\text{Bi}_2\text{Se}_3$  resulting in sputtering-induced reemergence of the topological state [21], which was initially strongly affected by the Gaussian disorder due to surface adsorbates.

In this regard, a future study of these high-quality annealed surfaces with x-ray reflectometry appears to be a natural extension of this study.

## VIII. SUMMARY

We performed soft x-ray absorption and reflectometry measurements on  $\text{SmB}_6$  samples cleaved at room temperature. Having ensured the stability of the cleaved surface we analyzed the absorption data at the  $M_{4,5}$  edge of Sm and showed that there are essentially only two types of Sm ions:  $\text{Sm}^{2+}$  and

$\text{Sm}^{3+}$ , which also suggested that there should be no Sm atoms at the very surface, as these would have different coordination. We used momentum- and energy-dependent reflectivity data to extract depth- and element-resolved chemical profiles for both B and Sm, which confirmed a boron domination at the laterally averaged surface. Knowing that there are only two types of Sm ions, separate profiles were extracted for each valency. To this end, the reflectometry data were backed up with a crystal-field calculation, used to model optical properties of the two different Sm ions at the  $M_{4,5}$  resonance. Ultimately, three spatial regions were identified before the bulk properties recover: a boron-rich topmost layer; an underlying boron-deficient  $\text{Sm}^{3+}$  layer; and an layer with a mild  $\text{Sm}^{3+}$  prevalence and slight boron deficiency. Irrespective of the initial termination, a boron termination is established eventually, although the time required may vary substantially. While at room temperature it takes less than 2 h, below 50 K the reconstruction occurs on a timescale of about 24 h. Thus, we conclude that a thermally activated process involving loss of surface Sm should stand behind the observed surface reconstruction.

We believe that the established chemical and valence profiles will be helpful for a better understanding and control of the surface polarity [26] and magnetism [35] in  $\text{SmB}_6$  and consequently in interpreting the emergence of surface states in this system [23,125].

## ACKNOWLEDGMENTS

V.B.Z. and K.F. would like to thank M. W. Haverkort for the insightful discussion and the introduction to CFT. C.H.M. thanks Diamond Light Source and especially T.-L. Lee and C. Schlueter for experimental support at beamline I09 (Grant No. SI14732). Likewise, C.H.M. thanks J. D. Denlinger and the beamline staff of MERLIN beamline 4.0.3 at Advanced Light Source, which is a DOE Office of Science User Facility under Contract No. DE-AC02-05CH11231. B.K.C. and B.Y.K. were supported by National Research Foundation of Korea (NRF) grants funded by the Ministry of Education (Grant No. NRF-2017R1A2B2008538) and Bank for Quantum Electronic Materials-BQEM000652. This work has been supported by the Max Planck-UBC Centre for Quantum Materials and by the German Research Foundation (DFG) through SFB 1170 “ToCoTronics” (Projects C04 and C06) and SFB 1143 “Correlated magnetism: From Frustration to Topology” (Project C03). D.S.I. acknowledges the DFG individual research Grant No. IN 209/3-2. Some experiments for this work were performed at the Canadian Light Source, which is funded by the Canada Foundation for Innovation, NSERC, the National Research Council of Canada, the Canadian Institutes of Health Research, the Government of Saskatchewan, Western Economic Diversification Canada, and the University of Saskatchewan.

- 
- [1] A. Menth, E. Buehler, and T. H. Geballe, *Phys. Rev. Lett.* **22**, 295 (1969).
  - [2] J. W. Allen, L. I. Johansson, I. Lindau, and S. B. Hagstrom, *Phys. Rev. B* **21**, 1335 (1980).
  - [3] J. M. Lawrence, P. S. Riseborough, and R. D. Parks, *Rep. Prog. Phys.* **44**, 1 (1981).
  - [4] T. Kasuya, *Europhys. Lett.* **26**, 283 (1994).
  - [5] G. Wertheim and M. Campagna, *Chem. Phys. Lett.* **47**, 182 (1977).
  - [6] G. Güntherodt, W. A. Thompson, F. Holtzberg, and Z. Fisk, *Phys. Rev. Lett.* **49**, 1030 (1982).
  - [7] G. Travaglini and P. Wachter, *Phys. Rev. B* **29**, 893 (1984).
  - [8] E. V. Sampathkumaran, *Hyperfine Interact.* **27**, 183 (1986).
  - [9] P. A. Alekseev, V. N. Lazukov, R. Osborn, B. D. Rainford, I. P. Sadikov, E. S. Kononova, and Y. B. Paderno, *Europhys. Lett.* **23**, 347 (1993).
  - [10] J. N. Chazalviel, M. Campagna, G. K. Wertheim, and P. H. Schmidt, *Phys. Rev. B* **14**, 4586 (1976).
  - [11] E. Beaupaire, J. P. Kappler, and G. Krill, *Phys. Rev. B* **41**, 6768 (1990).
  - [12] D. Mandrus, J. L. Sarrao, A. Lacerda, A. Migliori, J. D. Thompson, and Z. Fisk, *Phys. Rev. B* **49**, 16809 (1994).
  - [13] J. C. Cooley, M. C. Aronson, Z. Fisk, and P. C. Canfield, *Phys. Rev. Lett.* **74**, 1629 (1995).
  - [14] P. S. Riseborough, *Adv. Phys.* **49**, 257 (2000).
  - [15] M. Dzero, K. Sun, V. Galitski, and P. Coleman, *Phys. Rev. Lett.* **104**, 106408 (2010).
  - [16] F. Lu, J. Z. Zhao, H. Weng, Z. Fang, and X. Dai, *Phys. Rev. Lett.* **110**, 096401 (2013).
  - [17] M. Neupane, N. Alidoust, S. Xu, T. Kondo, Y. Ishida, D.-J. Kim, C. Liu, I. Belopolski, Y. Jo, T.-R. Chang *et al.*, *Nat. Commun.* **4**, 3991 (2013).
  - [18] J. Jiang, S. Li, T. Zhang, Z. Sun, F. Chen, Z. Ye, M. Xu, Q. Ge, S. Tan, X. Niu, H. Wen, and D. Feng, *Nat. Commun.* **4**, 3010 (2013).
  - [19] N. Xu, P. K. Biswas, J. H. Dil, R. S. Dhaka, G. Landolt, S. Muff, C. E. Matt, X. Shi, N. C. Plumb, M. Radovi *et al.*, *Nat. Commun.* **5**, 4566 (2014).
  - [20] D. J. Kim, J. Xia, and Z. Fisk, *Nat. Mater.* **13**, 466 (2014).
  - [21] R. Queiroz, G. Landolt, S. Muff, B. Slomski, T. Schmitt, V. N. Strocov, J. Mi, B. B. Iversen, P. Hofmann, J. Osterwalder, A. P. Schnyder, and J. H. Dil, *Phys. Rev. B* **93**, 165409 (2016).
  - [22] N. Wakeham, Y. Q. Wang, Z. Fisk, F. Ronning, and J. D. Thompson, *Phys. Rev. B* **91**, 085107 (2015).
  - [23] J. Kim, K. Kim, C.-J. Kang, S. Kim, H. C. Choi, J.-S. Kang, J. D. Denlinger, and B. I. Min, *Phys. Rev. B* **90**, 075131 (2014).
  - [24] P. Syers, D. Kim, M. S. Fuhrer, and J. Paglione, *Phys. Rev. Lett.* **114**, 096601 (2015).
  - [25] P. Hlawenka, K. Siemensmeyer, E. Weschke, A. Varykhalov, J. Sánchez-Barriga, N. Y. Shitsevalova, A. V. Dukhnenko, V. B. Filipov, S. Gabáni, K. Flachbart, O. Rader, and E. D. L. Rienks, *Nat. Commun.* **9**, 517 (2018).
  - [26] Z.-H. Zhu, A. Nicolaou, G. Levy, N. P. Butch, P. Syers, X. F. Wang, J. Paglione, G. A. Sawatzky, I. S. Elfimov, and A. Damascelli, *Phys. Rev. Lett.* **111**, 216402 (2013).
  - [27] E.-J. Cho and S.-J. Oh, *Phys. Rev. B* **59**, R15613(R) (1999).

- [28] W. A. Phelan, S. M. Koohpayeh, P. Cottingham, J. W. Freeland, J. C. Leiner, C. L. Broholm, and T. M. McQueen, *Phys. Rev. X* **4**, 031012 (2014).
- [29] J. W. Allen, *Philos. Mag.* **96**, 3227 (2016).
- [30] H. He, L. Miao, E. Augustin, J. Chiu, S. Wexler, S. A. Breitweiser, B. Kang, B. K. Cho, C.-H. Min, F. Reinert, Y.-D. Chuang, J. Denlinger, and L. A. Wray, *Phys. Rev. B* **95**, 195126 (2017).
- [31] J. D. Denlinger, J. W. Allen, J.-S. Kang, K. Sun, B.-I. Min, D.-J. Kim, and Z. Fisk, *JPS Conf. Proc.* **3**, 017038 (2014).
- [32] S. Rößler, L. Jiao, D. Kim, S. Seiro, K. Rasim, F. Steglich, L. Tjeng, Z. Fisk, and S. Wirth, *Philos. Mag.* **96**, 3262 (2016).
- [33] S. Rößler, T.-H. Jang, D.-J. Kim, L. H. Tjeng, Z. Fisk, F. Steglich, and S. Wirth, *Proc. Natl. Acad. Sci. USA* **111**, 4798 (2014).
- [34] L. Jiao, S. Rößler, D. Kim, L. Tjeng, Z. Fisk, F. Steglich, and S. Wirth, *Nat. Commun.* **7**, 13762 (2016).
- [35] P. K. Biswas, M. Legner, G. Balakrishnan, M. C. Hatnean, M. R. Lees, D. M. Paul, E. Pomjakushina, T. Prokscha, A. Suter, T. Neupert, and Z. Salman, *Phys. Rev. B* **95**, 020410 (2017).
- [36] P. Lutz, M. Thees, T. R. Peixoto, B. Y. Kang, B. K. Cho, C. H. Min, and F. Reinert, *Philos. Mag.* **96**, 3307 (2016).
- [37] N. Barrett, E. E. Krasovskii, J.-M. Themlin, and V. N. Strocov, *Phys. Rev. B* **71**, 035427 (2005).
- [38] J. Lobo-Checa, J. E. Ortega, A. Mascaraque, E. G. Michel, and E. E. Krasovskii, *Phys. Rev. B* **84**, 245419 (2011).
- [39] X.-L. Zhou and S.-H. Chen, *Phys. Rep.* **257**, 223 (1995).
- [40] S. Dietrich and A. Haase, *Phys. Rep.* **260**, 1 (1995).
- [41] D. G. Hawthorn, F. He, L. Venema, H. Davis, A. J. Achkar, J. Zhang, R. Sutarto, H. Wadati, A. Radi, T. Wilson, G. Wright, K. M. Shen, J. Geck, H. Zhang, V. Novák, and G. A. Sawatzky, *Rev. Sci. Instrum.* **82**, 073104 (2011).
- [42] G. Friemel, Y. Li, A. V. Dukhnenko, N. Y. Shitsevalova, N. E. Sluchanko, A. Ivanov, V. B. Filipov, B. Keimer, and D. S. Inosov, *Nat. Commun.* **3**, 830 (2012).
- [43] B. Y. Kang, C.-H. Min, S. S. Lee, M. S. Song, K. K. Cho, and B. K. Cho, *Phys. Rev. B* **94**, 165102 (2016).
- [44] S. de Jong, Ph.D. thesis, FNWI, Van der Waals-Zeeman Institute, University of Amsterdam, 2006.
- [45] V. B. Zabolotnyy, E. Carleschi, T. K. Kim, A. A. Kordyuk, J. Trinckauf, J. Geck, D. Evtushinsky, B. P. Doyle, R. Fittipaldi, M. Cuoco, A. Vecchione, B. Büchner, and S. V. Borisenko, *New J. Phys.* **14**, 063039 (2012).
- [46] F. Mercier-Bion, R. Drot, J. J. Ehrhardt, J. Lambert, J. Roques, and E. Simoni, *Surf. Interface Anal.* **43**, 777 (2011).
- [47] A. Hoffman and A. Laikhtman, *J. Phys.: Condens. Matter* **18**, S1517 (2006).
- [48] J. Chen, K. Lu, J. Lee, and S. Haw, *Surf. Sci.* **600**, 3544 (2006).
- [49] G. Loubriel and C. Parks, *J. Less Common Met.* **93**, 213 (1983).
- [50] M. L. Knotek and P. J. Feibelman, *Phys. Rev. Lett.* **40**, 964 (1978).
- [51] L. Dudy, M. Sing, P. Scheiderer, J. D. Denlinger, P. Schütz, J. Gabel, M. Buchwald, C. Schlueter, T.-L. Lee, and R. Claessen, *Adv. Mater.* **28**, 7443 (2016).
- [52] S. M. Walker, F. Y. Bruno, Z. Wang, A. de la Torre, S. Riccò, A. Tamai, T. K. Kim, M. Hoesch, M. Shi, M. S. Bahramy, P. D. C. King, and F. Baumberger, *Adv. Mater.* **27**, 3894 (2015).
- [53] K. Hagiwara, Y. Ohtsubo, M. Matsunami, S.-i. Ideta, K. Tanaka, H. Miyazaki, J. E. Rault, P. L. Fare, F. Bertran, A. Taleb-Ibrahimi, R. Yukawa, M. Kobayashi, K. Horiba, H. Kumigashira, K. Sumida, T. Okuda, F. Iga, and S.-i. Kimura, *Nat. Commun.* **7**, 12690 (2016).
- [54] B. T. Thole, G. van der Laan, J. C. Fuggle, G. A. Sawatzky, R. C. Karnatak, and J.-M. Esteve, *Phys. Rev. B* **32**, 5107 (1985).
- [55] J. E. Castle and A. M. Salvi, *J. Vac. Sci. Technol. A* **19**, 1170 (2001).
- [56] C.-H. Min, O. Sommer, B. Kang, B. Cho, H. Bentmann, and F. Reinert, *J. Electron Spectrosc. Relat. Phenom.* **199**, 46 (2015).
- [57] P. P. Mitra, S. Ogawa, X. Hu, and K. Ugurbil, *Magn. Reson. Med.* **37**, 511 (1997).
- [58] E. C. Landahl and S. E. Rice, *Phys. Rev. E* **88**, 062713 (2013).
- [59] H. Ade and A. P. Hitchcock, *Polymer* **49**, 643 (2008).
- [60] V. A. Marčenko and L. A. Pastur, *Mat. Sb. (N.S.)* **72**, 507 (1967) [*Math. USSR Sb.* **1**, 457 (1967)].
- [61] A. I. Mees, P. E. Rapp, and L. S. Jennings, *Phys. Rev. A* **36**, 340 (1987).
- [62] C. Eckart and G. Young, *Psychometrika* **1**, 211 (1936).
- [63] M. Pompa, A. M. Flank, P. Lagarde, J. C. Rife, I. Stekhin, M. Nakazawa, H. Ogasawara, and A. Kotani, *Phys. Rev. B* **56**, 2267 (1997).
- [64] R. Nakajima, J. Stöhr, and Y. U. Idzerda, *Phys. Rev. B* **59**, 6421 (1999).
- [65] A. J. Achkar, T. Z. Regier, H. Wadati, Y.-J. Kim, H. Zhang, and D. G. Hawthorn, *Phys. Rev. B* **83**, 081106 (2011).
- [66] R. Kurian, K. Kunnus, P. Wernet, S. M. Butorin, P. Glatzel, and F. M. F. de Groot, *J. Phys.: Condens. Matter* **24**, 452201 (2012).
- [67] H. Henneken, F. Scholze, and G. Ulm, *J. Appl. Phys.* **87**, 257 (2000).
- [68] S. Gota, M. Gautier-Soyer, and M. Sacchi, *Phys. Rev. B* **62**, 4187 (2000).
- [69] B. T. Thole and G. van der Laan, *Phys. Rev. B* **38**, 3158 (1988).
- [70] J. E. Hamann-Borrero, S. Macke, W. S. Choi, R. Sutarto, F. He, A. Radi, I. Elfimov, R. J. Green, M. W. Haverkort, V. B. Zabolotnyy, H. N. Lee, G. A. Sawatzky, and V. Hinkov, *npj Quantum Mater.* **1**, 16013 (2016).
- [71] X. Zhang, N. P. Butch, P. Syers, S. Ziemak, R. L. Greene, and J. Paglione, *Phys. Rev. X* **3**, 011011 (2013).
- [72] E. Frantzeskakis, N. de Jong, B. Zwartsenberg, Y. K. Huang, Y. Pan, X. Zhang, J. X. Zhang, F. X. Zhang, L. H. Bao, O. Tegus, A. Varykhalov, A. de Visser, and M. S. Golden, *Phys. Rev. X* **3**, 041024 (2013).
- [73] S. J. Oh and S. Doniach, *Phys. Rev. B* **26**, 2085 (1982).
- [74] C. J. Ballhausen, *Ligand Field Theory*, Vol. 256 (McGraw-Hill, New York, 1962).
- [75] R. D. Cowan, *The Theory of Atomic Structure and Spectra*, Vol. 3 (University of California Press, Berkeley, CA, 1981).
- [76] V. I. Anisimov and O. Gunnarsson, *Phys. Rev. B* **43**, 7570 (1991).
- [77] M. Sundermann, H. Yavaş, K. Chen, D. J. Kim, Z. Fisk, D. Kasinathan, M. W. Haverkort, P. Thalmeier, A. Severing, and L. H. Tjeng, *Phys. Rev. Lett.* **120**, 016402 (2018).
- [78] E. Zirngiebl, B. Hillebrands, S. Blumenröder, G. Güntherodt, M. Loewenhaupt, J. M. Carpenter, K. Winzer, and Z. Fisk, *Phys. Rev. B* **30**, 4052 (1984).
- [79] M. Loewenhaupt, J. Carpenter, and C.-K. Loong, *J. Magn. Magn. Mater.* **52**, 245 (1985).
- [80] A. S. Cameron, G. Friemel, and D. S. Inosov, *Rep. Prog. Phys.* **79**, 066502 (2016).

- [81] J. C. Nickerson, R. M. White, K. N. Lee, R. Bachmann, T. H. Geballe, and G. W. Hull, *Phys. Rev. B* **3**, 2030 (1971).
- [82] V. N. Antonov, B. N. Harmon, and A. N. Yaresko, *Phys. Rev. B* **66**, 165209 (2002).
- [83] A. B. Shick, L. Havela, A. I. Lichtenstein, and M. I. Katsnelson, *Sci. Rep.* **5**, 15429 (2015).
- [84] M. W. Haverkort, <http://www.quanty.org/>
- [85] M. W. Haverkort, *J. Phys.: Conf. Ser.* **712**, 012001 (2016).
- [86] M. W. Haverkort, M. Zwierzycki, and O. K. Andersen, *Phys. Rev. B* **85**, 165113 (2012).
- [87] Y. Lu, M. Höppner, O. Gunnarsson, and M. W. Haverkort, *Phys. Rev. B* **90**, 085102 (2014).
- [88] M. W. Haverkort, G. Sangiovanni, P. Hansmann, A. Toschi, Y. Lu, and S. Macke, *Europhys. Lett.* **108**, 57004 (2014).
- [89] P. Thunström, I. Di Marco, A. Grechnev, S. Lebègue, M. I. Katsnelson, A. Svane, and O. Eriksson, *Phys. Rev. B* **79**, 165104 (2009).
- [90] P. A. Alekseev, J. M. Mignot, J. Rossat-Mignod, V. N. Lazukov, I. P. Sadikov, E. S. Konovalova, and Y. B. Paderno, *J. Phys.: Condens. Matter* **7**, 289 (1995).
- [91] E. V. Nefedova, P. A. Alekseev, E. S. Klement'ev, V. N. Lazukov, I. P. Sadikov, M. N. Khlopkin, M. B. Tsetlin, E. S. Konovalova, and Y. B. Paderno, *J. Exp. Theor. Phys.* **88**, 565 (1999).
- [92] H. Ebel, *Powder Diffr.* **19**, 90 (2004).
- [93] B. H. Frazer, B. Gilbert, B. R. Sonderegger, and G. D. Stasio, *Surf. Sci.* **537**, 161 (2003).
- [94] S. Schroeder, G. Moggridge, R. Ormerod, T. Rayment, and R. Lambert, *Surf. Sci.* **324**, L371 (1995).
- [95] S. Macke, A. Radi, J. E. Hamann-Borrero, A. Verna, M. Bluschke, S. Brück, E. Goering, R. Sutarto, F. He, G. Cristiani *et al.*, *Adv. Mater.* **26**, 6554 (2014).
- [96] M. Nayak and G. S. Lodha, *J. Appl. Phys.* **114**, 023505 (2013).
- [97] M. Nayak, P. C. Pradhan, and G. S. Lodha, *J. Appl. Crystallogr.* **48**, 786 (2015).
- [98] E. O. Filatova, A. A. Sokolov, I. V. Kozhevnikov, E. Y. Taracheva, O. S. Grunsky, F. Schaefers, and W. Braun, *J. Phys.: Condens. Matter* **21**, 185012 (2009).
- [99] E. Benckiser, M. W. Haverkort, S. Brück, E. Goering, S. Macke, A. Frañó, X. Yang, O. K. Andersen, G. Cristiani, H.-U. Habermeier, A. V. Boris, I. Zegkinoglou, P. Wochner, H.-J. Kim, V. Hinkov, and B. Keimer, *Nat. Mater.* **10**, 189 (2011).
- [100] J. Fink, E. Schierle, E. Weschke, and J. Geck, *Rep. Prog. Phys.* **76**, 056502 (2013).
- [101] C. T. Chantler, *J. Phys. Chem. Ref. Data* **24**, 71 (1995).
- [102] L. G. Parratt, *Phys. Rev.* **95**, 359 (1954).
- [103] M. Björck and G. Andersson, *J. Appl. Crystallogr.* **40**, 1174 (2007).
- [104] R. Storn and K. Price, *J. Global Optim.* **11**, 341 (1997).
- [105] P. A. Alekseev, A. S. Ivanov, B. Dorner, H. Schober, K. A. Kikoin, A. S. Mishchenko, V. N. Lazukov, E. S. Konovalova, Y. B. Paderno, A. Y. Rumyantsev, and I. P. Sadikov, *Europhys. Lett.* **10**, 457 (1989).
- [106] V. A. Trounov, A. L. Malyshev, D. Y. Chernyshov, M. M. Korsukova, V. N. Gurin, L. A. Aslanov, and V. V. Chernyshev, *J. Phys.: Condens. Matter* **5**, 2479 (1993).
- [107] E. Vainshtein, S. Blokhin, and Y. B. Paderno, *Fizika Tverdogo Tela* **6**, 2909 (1964)[*Sov. Phys.-Solid State* **6**, 2318 (1965)].
- [108] R. L. Cohen, M. Eibschütz, and K. W. West, *Phys. Rev. Lett.* **24**, 383 (1970).
- [109] J.-M. Tarascon, Y. Isikawa, B. Chevalier, J. Etourneau, P. Hagenmuller, and M. Kasaya, *J. Phys.* **41**, 1141 (1980).
- [110] Y. S. Grushko, Y. B. Paderno, K. Ya. Mishin, L. I. Molkanov, G. A. Shadrina, E. S. Konovalova, and E. M. Dudnik, *Phys. Status Solidi B* **128**, 591 (1985).
- [111] Y. Utsumi, D. Kasinathan, K.-T. Ko, S. Agrestini, M. W. Haverkort, S. Wirth, Y.-H. Wu, K.-D. Tsuei, D.-J. Kim, Z. Fisk, A. Tanaka, P. Thalmeier, and L. H. Tjeng, *Phys. Rev. B* **96**, 155130 (2017).
- [112] D. W. Johnson, *J. Phys. A: Math. Gen.* **8**, 490 (1975).
- [113] W. Ruan, C. Ye, M. Guo, F. Chen, X. Chen, G.-M. Zhang, and Y. Wang, *Phys. Rev. Lett.* **112**, 136401 (2014).
- [114] N. Heming, U. Treske, M. Knupfer, B. Büchner, D. S. Inosov, N. Y. Shitsevalova, V. B. Filipov, S. Krause, and A. Koitzsch, *Phys. Rev. B* **90**, 195128 (2014).
- [115] M. Aono, R. Nishitani, C. Oshima, T. Tanaka, E. Bannai, and S. Kawai, *Surf. Sci.* **86**, 631 (1979).
- [116] F. Reinert, R. Claessen, G. Nicolay, D. Ehm, S. Hüfner, W. P. Ellis, G.-H. Gweon, J. W. Allen, B. Kindler, and W. Assmus, *Phys. Rev. B* **58**, 12808 (1998).
- [117] H. Miyazaki, T. Hajiri, T. Ito, S. Kunii, and S.-I. Kimura, *Phys. Rev. B* **86**, 075105 (2012).
- [118] M. Ellguth, C. Tusche, F. Iga, and S. Suga, *Philos. Mag.* **96**, 3284 (2016).
- [119] T. Miyamachi, S. Suga, M. Ellguth, C. Tusche, C. M. Schneider, F. Iga, and F. Komori, *Sci. Rep.* **7**, 12837 (2017).
- [120] H. Oechsner, *Appl. Phys.* **8**, 185 (1975).
- [121] G. Carter and R. Webb, *Radiat. Eff.* **37**, 21 (1978).
- [122] A. Vehanen, P. Huttunen, J. Mäkinen, and P. Hautojärvi, *J. Vac. Sci. Technol. A* **5**, 1142 (1987).
- [123] J. Bremer, J.-K. Hansen, and O. Hunderi, *Surf. Sci.* **436**, L735 (1999).
- [124] A. Moreno-Barrado, R. Gago, A. Redondo-Cubero, L. Vázquez, J. Muñoz-García, R. Cuerno, K. Lorenz, and M. Castro, *Europhys. Lett.* **109**, 48003 (2015).
- [125] M. Trenary, *Sci. Technol. Adv. Mater.* **13**, 023002 (2012).